The Astrophysical Journal, 944:43 (10pp), 2023 February 10 https://doi.org/10.3847/1538-4357/aca9d1

Timing the *r*-process Enrichment of the Ultra-faint Dwarf Galaxy Reticulum II

Joshua D. Simon[1], Thomas M. Brown[2], Burçin Mutlu-Pakdil[3,4,5], Alexander P. Ji[3,4], Alex Drlica-Wagner[3,4,6], Roberto J. Avila[2], Clara E. Martínez-Vázquez[7], Ting S. Li[8], Eduardo Balbinot[9], Keith Bechtol[10], Anna Frebel[11,12], Marla Geha[13], Terese T. Hansen[14], David J. James[15], Andrew B. Pace[16], M. Aguena[17], O. Alves[18], F. Andrade-Oliveira[18], J. Annis[6], D. Bacon[19], E. Bertin[20,21], D. Brooks[22], D. L. Burke[23,24], A. Carnero Rosell[17,25,26], M. Carrasco Kind[27,28], J. Carretero[29], M. Costanzi[30,31,32], L. N. da Costa[17], J. De Vicente[33], S. Desai[34], P. Doel[22], S. Everett[35], I. Ferrero[36], J. Frieman[3,6], J. García-Bellido[37], M. Gatti[38], D. W. Gerdes[18,39], D. Gruen[40], R. A. Gruendl[27,28], J. Gschwend[17,41], G. Gutierrez[6], S. R. Hinton[42], D. L. Hollowood[43], K. Honscheid[44,45], K. Kuehn[46,47], N. Kuropatkin[6], J. L. Marshall[48], J. Mena-Fernández[33], R. Miquel[29,49], A. Palmese[50], F. Paz-Chinchón[27,51], M. E. S. Pereira[52], A. Pieres[17,41], A. A. Plazas Malagón[53], M. Raveri[38], M. Rodriguez-Monroy[33], E. Sanchez[33], B. Santiago[17,54], V. Scarpine[6], I. Sevilla-Noarbe[33], M. Smith[55], E. Suchyta[56], M. E. C. Swanson, G. Tarle[18], C. To[44], M. Vincenzi[19,55], N. Weaverdyck[18,57], and R. D. Wilkinson[58]

[1] Observatories of the Carnegie Institution for Science, 813 Santa Barbara Steet, Pasadena, CA 91101, USA
[2] Space Telescope Science Institute, 3700 San Martin Drive, Baltimore, MD 21218, USA
[3] Kavli Institute for Cosmological Physics, University of Chicago, Chicago, IL 60637, USA
[4] Department of Astronomy and Astrophysics, University of Chicago, Chicago, IL 60637, USA
[5] Department of Physics and Astronomy, Dartmouth College, 6127 Wilder Laboratory, Hanover, NH 03755, USA
[6] Fermi National Accelerator Laboratory, P.O. Box 500, Batavia, IL 60510, USA
[7] Gemini Observatory, NSF's NOIRLaboratory, 670 N. A'ohoku Place, Hilo, HI 96720, USA
[8] Department of Astronomy and Astrophysics, University of Toronto, 50 St. George Street, Toronto, ON M5S 3H4, Canada
[9] Kapteyn Astronomical Institute, University of Groningen, Landleven 12, 9747 AD Groningen, The Netherlands
[10] Department of Physics, University of Wisconsin–Madison, Madison, WI 53706, USA
[11] Department of Physics & Kavli Institute for Astrophysics and Space Research, Massachusetts Institute of Technology, Cambridge, MA 02139, USA
[12] Joint Institute for Nuclear Astrophysics—Center for Evolution of the Elements, East Lansing, MI 48824, USA
[13] Department of Astronomy, Yale University, 52 Hillhouse Avenue, New Haven, CT 06520, USA
[14] Department of Astronomy, Stockholm University, AlbaNova University Centre, SE-106 91 Stockholm, Sweden
[15] Center for Astrophysics | Harvard & Smithsonian, 60 Garden Street, Cambridge, MA 02138, USA
[16] McWilliams Center for Cosmology, Carnegie Mellon University, 5000 Forbes Avenue, Pittsburgh, PA 15213, USA
[17] Laboratório Interinstitucional de e-Astronomia—LIneA, Rua Gal. José Cristino 77, Rio de Janeiro, RJ—20921-400, Brazil
[18] Department of Physics, University of Michigan, Ann Arbor, MI 48109, USA
[19] Institute of Cosmology and Gravitation, University of Portsmouth, Portsmouth, PO1 3FX, UK
[20] CNRS, UMR 7095, Institut d'Astrophysique de Paris, F-75014 Paris, France
[21] Sorbonne Universités, UPMC Univ Paris 06, UMR 7095, Institut d'Astrophysique de Paris, F-75014 Paris, France
[22] Department of Physics & Astronomy, University College London, Gower Street, London, WC1E 6BT, UK
[23] Kavli Institute for Particle Astrophysics & Cosmology, P.O. Box 2450, Stanford University, Stanford, CA 94305, USA
[24] SLAC National Accelerator Laboratory, Menlo Park, CA 94025, USA
[25] Instituto de Astrofisica de Canarias, E-38205 La Laguna, Tenerife, Spain
[26] Universidad de La Laguna, Dpto. Astrofísica, E-38206 La Laguna, Tenerife, Spain
[27] Center for Astrophysical Surveys, National Center for Supercomputing Applications, 1205 West Clark Street, Urbana, IL 61801, USA
[28] Department of Astronomy, University of Illinois at Urbana-Champaign, 1002 W. Green Street, Urbana, IL 61801, USA
[29] Institut de Física d'Altes Energies (IFAE), The Barcelona Institute of Science and Technology, Campus UAB, E-08193 Bellaterra (Barcelona) Spain
[30] Astronomy Unit, Department of Physics, University of Trieste, via Tiepolo 11, I-34131 Trieste, Italy
[31] INAF-Osservatorio Astronomico di Trieste, via G.B. Tiepolo 11, I-34143 Trieste, Italy
[32] Institute for Fundamental Physics of the Universe, Via Beirut 2, I-34014 Trieste, Italy
[33] Centro de Investigaciones Energéticas, Medioambientales y Tecnológicas (CIEMAT), Madrid, Spain
[34] Department of Physics, IIT Hyderabad, Kandi, Telangana 502285, India
[35] Jet Propulsion Laboratory, California Institute of Technology, 4800 Oak Grove Drive, Pasadena, CA 91109, USA
[36] Institute of Theoretical Astrophysics, University of Oslo, P.O. Box 1029 Blindern, NO-0315 Oslo, Norway
[37] Instituto de Fisica Teorica UAM/CSIC, Universidad Autonoma de Madrid, E-28049 Madrid, Spain
[38] Department of Physics and Astronomy, University of Pennsylvania, Philadelphia, PA 19104, USA
[39] Department of Astronomy, University of Michigan, Ann Arbor, MI 48109, USA
[40] University Observatory, Faculty of Physics, Ludwig-Maximilians-Universität, Scheinerstr. 1, D-81679 Munich, Germany
[41] Observatório Nacional, Rua Gal. José Cristino 77, Rio de Janeiro, RJ—20921-400, Brazil
[42] School of Mathematics and Physics, University of Queensland, Brisbane, QLD 4072, Australia
[43] Santa Cruz Institute for Particle Physics, Santa Cruz, CA 95064, USA
[44] Center for Cosmology and Astro-Particle Physics, The Ohio State University, Columbus, OH 43210, USA
[45] Department of Physics, The Ohio State University, Columbus, OH 43210, USA
[46] Australian Astronomical Optics, Macquarie University, North Ryde, NSW 2113, Australia
[47] Lowell Observatory, 1400 Mars Hill Road, Flagstaff, AZ 86001, USA
[48] George P. and Cynthia Woods Mitchell Institute for Fundamental Physics and Astronomy, and Department of Physics and Astronomy, Texas A&M University, College Station, TX 77843, USA
[49] Institució Catalana de Recerca i Estudis Avançats, E-08010 Barcelona, Spain
[50] Department of Astronomy, University of California, Berkeley, 501 Campbell Hall, Berkeley, CA 94720, USA
[51] Institute of Astronomy, University of Cambridge, Madingley Road, Cambridge, CB3 0HA, UK
[52] Hamburger Sternwarte, Universität Hamburg, Gojenbergsweg 112, D-21029 Hamburg, Germany
[53] Department of Astrophysical Sciences, Princeton University, Peyton Hall, Princeton, NJ 08544, USA
[54] Instituto de Física, UFRGS, Caixa Postal 15051, Porto Alegre, RS—91501-970, Brazil
[55] School of Physics and Astronomy, University of Southampton, Southampton, SO17 1BJ, UK
[56] Computer Science and Mathematics Division, Oak Ridge National Laboratory, Oak Ridge, TN 37831, USA

[57] Lawrence Berkeley National Laboratory, 1 Cyclotron Road, Berkeley, CA 94720, USA
[58] Department of Physics and Astronomy, Pevensey Building, University of Sussex, Brighton, BN1 9QH, UK
Received 2022 October 4; revised 2022 November 17; accepted 2022 November 30; published 2023 February 10

Abstract

The ultra-faint dwarf galaxy Reticulum II (Ret II) exhibits a unique chemical evolution history, with 72^{+10}_{-12}% of its stars strongly enhanced in *r*-process elements. We present deep Hubble Space Telescope photometry of Ret II and analyze its star formation history. As in other ultra-faint dwarfs, the color–magnitude diagram is best fit by a model consisting of two bursts of star formation. If we assume that the bursts were instantaneous, then the older burst occurred around the epoch of reionization, forming ∼80% of the stars in the galaxy, while the remainder of the stars formed ∼3 Gyr later. When the bursts are allowed to have nonzero durations, we obtain slightly better fits. The best-fitting model in this case consists of two bursts beginning before reionization, with approximately half the stars formed in a short (100 Myr) burst and the other half in a more extended period lasting 2.6 Gyr. Considering the full set of viable star formation history models, we find that 28% of the stars formed within 500 ± 200 Myr of the onset of star formation. The combination of the star formation history and the prevalence of *r*-process-enhanced stars demonstrates that the *r*-process elements in Ret II must have been synthesized early in its initial star-forming phase. We therefore constrain the delay time between the formation of the first stars in Ret II and the *r*-process nucleosynthesis to be less than 500 Myr. This measurement rules out an *r*-process source with a delay time of several Gyr or more, such as GW170817.

Unified Astronomy Thesaurus concepts: Dwarf galaxies (416); Local Group (929); Stellar populations (1622); Galaxy ages (576); HST photometry (756); Nucleosynthesis (1131); R-process (1324)

Supporting material: machine-readable table

1. Introduction

Identifying the astrophysical production site of the *r*-process elements has been a long-standing goal of studies of chemical evolution and nuclear astrophysics (e.g., Frebel 2018 and references therein). At the broadest level, the debate is between rare events producing large quantities of *r*-process material and frequent events producing small amounts of *r*-process elements. The former category includes neutron star mergers (e.g., Lattimer & Schramm 1974; Meyer 1989), jet-driven supernovae (SNe; e.g., Cameron 2003; Fujimoto et al. 2008; Halevi & Mosta 2018), and, more recently, collapsars (e.g., MacFadyen & Woosley 1999; Surman et al. 2006; Siegel et al. 2019), while the latter is usually assumed to relate to ordinary core-collapse SN explosions (e.g., Burbidge et al. 1957; Arcones & Thielemann 2013).

The discovery of the strongly *r*-process-enhanced stars ([Eu/Fe] > 1.0) in the ultra-faint dwarf (UFD) galaxy Reticulum II (Ret II) provided decisive evidence in favor of a rare and prolific source of *r*-process elements (Ji et al. 2016a; Roederer et al. 2016). The subsequent confirmation of *r*-process nucleosynthesis in the neutron star merger GW170817 (Chornock et al. 2017; Drout et al. 2017; Kasliwal et al. 2017; Pian et al. 2017; Tanvir et al. 2017) then made a strong case that the rare and prolific source should be identified with merging neutron stars. However, the story is not necessarily over. The combination of the short expected timescale for star formation in Ret II and the potentially long delay time between star formation and a neutron star merger remains a challenge to understand. Specifically, although the core-collapse explosions of massive stars occur within a few million yr of the births of those stars, binary neutron star systems may take hundreds of Myr or even longer to merge (e.g., Dominik et al. 2012). The relative importance of neutron star mergers and rapid sources—such as collapsars and jet-driven SNe—to *r*-process nucleosynthesis also remains controversial (e.g., Bartos & Márka 2019; Siegel et al. 2019; Brauer et al. 2021; Reggiani et al. 2021; Fraser & Schonrich 2022). And the low but nonzero levels of *r*-process enrichment in other UFDs appear to require a second source (presumably core-collapse SNe) of *r*-process material as well (e.g., Frebel et al. 2010, 2014; Ishigaki et al. 2014; Ji et al. 2016b).

Dwarf galaxies provide clean environments for unraveling early galactic chemical evolution, because of the limited number of nucleosynthetic events that enriched their oldest stars (e.g., Simon et al. 2015b; Chiaki & Wise 2019; Hartwig et al. 2019) and because each dwarf is the descendant of relatively few progenitor systems (Fitts et al. 2018; Griffen et al. 2018). Ret II is particularly interesting in this regard, as 72^{+10}_{-12}% of its stars are *r*-process-enhanced (Ji et al. 2016a, 2016c, 2022). The non-*r*-process-enhanced fraction is thus 28^{+12}_{-10}%. This result demonstrates that the event that produced the *r*-process elements in Ret II must have occurred at a time when no more than 28% of the galaxy's stars had formed. Given the contrast in timescales between different candidate *r*-process sites, determining the star formation history (SFH) of Ret II therefore offers the possibility of placing a limit on the timescale of *r*-process enrichment in the galaxy, which could enable a prompt or delayed source for the *r*-process elements to be distinguished.

The stellar populations of the UFDs that have been examined thus far are exclusively old, with typical ages of ∼13 Gyr (Brown et al. 2012, 2014). However, there is tentative evidence for some differences in detail from galaxy to galaxy. For example, Ursa Major I may exhibit a longer duration of star formation and a younger mean age than the other UFDs in the Brown et al. (2014) sample, most notably Canes Venatici II (CVn II) and Coma Berenices (Com), as well as, to a lesser extent, Boötes I, Hercules, and Leo IV. Intriguingly, Sacchi et al. (2021) also detected a possible difference in mean age between satellites of the Magellanic Clouds (including Ret II)

and satellites of the Milky Way, with the star formation in the former systems ending 600 Myr later.

The Sacchi et al. (2021) SFH for Ret II is based on imaging of a single Hubble Space Telescope (HST) pointing that covers a small fraction of the galaxy and therefore contains fewer than 200 Ret II stars (∼2% of the total stellar content, assuming the stellar mass of 3300 $M_{\odot}$ from Ji et al. 2022 and the initial mass function from Safarzadeh et al. 2022). In this paper, we present a SFH analysis of Ret II from wider-area HST imaging with a substantially larger sample of stars (∼2600 Ret II members; ∼25% of the stars in the galaxy). In Section 2, we describe our observations and the data reduction and photometry procedures. In Section 3, we determine the SFH of Ret II. We discuss the implications of the SFH for *r*-process nucleosynthesis in Section 4, and we summarize our results and conclusions in Section 5.

2. HST Data

2.1. Observations

We obtained a 12-tile mosaic of Ret II with the Wide Field Channel of the Advanced Camera for Surveys (ACS; Ford et al. 2003) on HST, through program GO-14766 (PI: Simon). The observations were carried out between 2016 November 9 and 2016 November 26.

Given the proximity of Ret II to the Milky Way, even short integration times enabled us to exceed the target signal-to-noise ratio (S/N) of 100 at 1 mag below the oldest main-sequence turnoff (MSTO), which occurs at $m_{814} \approx 23.5$ at the distance of Ret II. Each mosaic tile was observed for a single orbit, consisting of two F606W exposures and two F814W exposures, with total integration times of 980 s in F606W and 1140 s in F814W. A 3.″034 dither was performed between the first and second exposures in each filter, to fill in the gap between the ACS chips and to reject cosmic rays. In previous UFD programs with HST (Brown et al. 2014; Simon et al. 2021), we used a four-point dither pattern to fully sample the ACS point-spread function (PSF). However, CCD readout constraints make it impossible to obtain eight exposures across multiple filters in one HST orbit, so additional dither positions would have required doubling the number of orbits devoted to the project or halving the area covered. Being limited to two dithered exposures per band has implications for the photometric methods employed, as discussed below, but was workable, given the low surface density of the stars in Ret II.

Based on the distribution of Ret II member stars in the initial Dark Energy Survey data (Bechtol et al. 2015; Drlica-Wagner et al. 2018), the mosaic tiles were arranged in an elongated east–west pattern, to completely cover the area within the half-light radius of Ret II. The main east–west mosaic pattern included only one blue horizontal branch (BHB) star from the spectroscopic sample of Simon et al. (2015a), so one ACS tile was placed in the northeast corner of the mosaic to observe a second BHB star, in order to better constrain the distance of Ret II. The spatial coverage of the observations is shown in Figure 1 of Safarzadeh et al. (2022).

2.2. Reduction and Photometry

Our initial data reduction procedures followed those described by Brown et al. (2014) and Simon et al. (2021). We processed the raw images with the most recent version of the ACS pipeline, including bias subtraction, dark subtraction, identification of detector artifacts, and charge transfer efficiency correction. The images were resampled onto a 0.″035 pixel grid, with each tile covering an area of approximately 200″ × 205″, with overlaps of a few arcseconds between adjacent tiles.

We performed PSF photometry on the pipeline-produced, flat-fielded, charge transfer efficiency–corrected (FLC) images, with the latest version (2.0) of DOLPHOT (Dolphin 2000), as in Mutlu-Pakdil et al. (2019, 2020). We followed the recommended preprocessing steps and used the suggested input parameters from the DOLPHOT User Guide.[59] The initial photometry was then cleaned of spurious detections using the following criteria: the sum of the crowding parameters in the two bands must be <1, the squared sum of the sharpness parameters in the two bands must be <0.1, and the S/N must be ⩾4 and the object-type[60] must be ⩽2 in each band. The resulting color–magnitude diagram (CMD) is displayed in Figure 1, and Table 1 contains the cleaned photometric catalog.

We carried out artificial star tests, in order to quantify the photometric uncertainties and completeness in our observations, using the artificial star utilities in DOLPHOT. We injected a total of ∼5 million artificial stars per tile, distributing them evenly across the field of view. Because each star was inserted and photometered one at a time, the large number of stars inserted during the artificial star tests did not cause any self-induced crowding (Dolphin 2000). The input colors and magnitudes of the artificial stars covered the complete range of the observed colors and magnitudes (i.e., $18 \leqslant m_{606} \leqslant 30$ and $-0.75 \leqslant m_{606} - m_{814} \leqslant 2.0$). Photometry and quality cuts were performed in an identical manner to those performed on the original photometry.

The two BHB stars mentioned in Section 2.1 were saturated in the drizzled images. Because these stars are important for determining the distance of Ret II (Section 3.1), we used aperture photometry on the individual FLC exposures to recover their fluxes by hand. The instrumental magnitudes measured in this way from the two separate exposures per band in each tile agreed to better than 0.01 mag for each star, indicating that the photometric precision for these stars remains high, despite the saturation effects.

We note that in previous SFH analyses by our group (e.g., Brown et al. 2014; Simon et al. 2021), we have relied on PSF-fitting photometry, using the DAOPHOT-II package (Stetson 1987). With this data set, applying the same procedures that we had used in the past resulted in unexpected artifacts in the CMD, most notably an increased width of the main sequence (MS), which were not present in the photometry carried out with DOLPHOT. The difference between the DAOPHOT and DOLPHOT results appears to be a consequence of the incomplete sampling of the PSF from having only two dither positions as well as the sparseness of the field. In this regime, the empirical PSF library used by DOLPHOT is more appropriate than a PSF model constructed directly from the data in DAOPHOT.

[59] http://americano.dolphinsim.com/dolphot/dolphotACS.pdf

[60] This parameter distinguishes point sources from extended sources and artifacts, as described in the DOLPHOT manual.

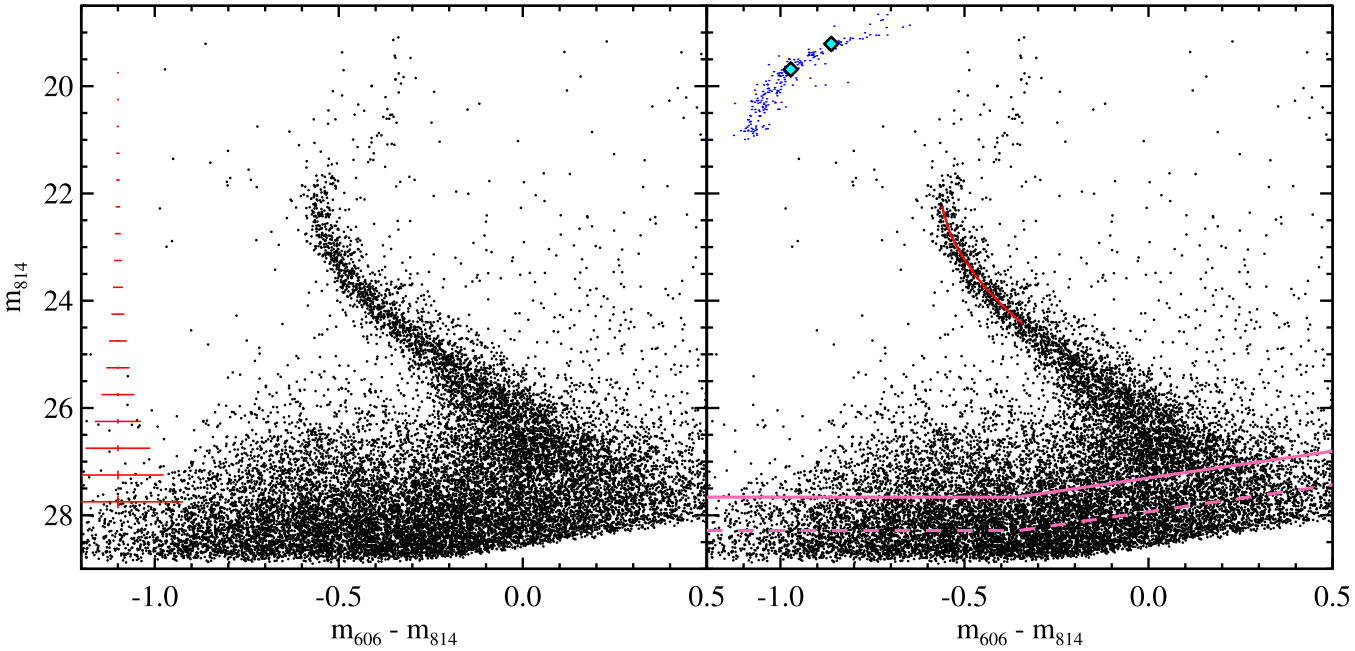

Figure 1. (Left) ACS color–magnitude diagram of Ret II. Magnitude measurements are in the STMAG system, and only stars meeting the criteria described in Section 2.2 are included. The two stars closest to the upper left corner are the BHB members of Ret II. Typical photometric uncertainties as a function of magnitude are plotted in red along the left of the figure. (Right) Ret II color–magnitude diagram, as in the left panel, with the M92 horizontal branch (blue dots in upper left) and the upper main sequence portion of the Victoria-Regina isochrone (red curve) overlaid, both shifted to the best-fit distance and reddening for Ret II. The Ret II BHB stars are highlighted with cyan diamonds. The 90% and 50% completeness limits are displayed as solid and dashed pink lines, respectively.

Table 1
Ret II Stellar Photometry

Star	R.A. (J2000)	Decl. J2000)	m_{606}	δm_{606}	m_{814}	δm_{814}
1	54.123158	−53.961302	20.233	0.002	19.410	0.002
2	54.108976	−53.968195	20.201	0.002	20.081	0.002
3	54.132862	−53.957064	21.105	0.003	19.781	0.001
4	54.102355	−53.948340	20.669	0.002	20.271	0.002
5	54.086859	−53.943280	21.470	0.003	20.241	0.002
6	54.123401	−53.946231	20.995	0.003	21.415	0.003
7	54.149917	−53.941306	21.129	0.003	21.503	0.003
8	54.143632	−53.958409	22.183	0.005	20.967	0.003
9	54.134904	−53.966469	22.181	0.005	21.030	0.002
10	54.059216	−53.967990	21.897	0.004	21.208	0.003

Note. The magnitudes are on the STMAG system and the astrometry is calibrated to Gaia data release 3 (Gaia Collaboration et al. 2022).

(This table is available in its entirety in machine-readable form.)

3. The SFH of Ret II

3.1. Metallicity Distribution, Distance, and Reddening

Before modeling the SFH of Ret II, we first determined the distance of the galaxy, the foreground reddening, and the metallicity distribution, in order to be able to compare theoretical stellar isochrones with the HST photometry.

Distances to Local Group dwarf galaxies are typically best determined with RR Lyrae variable stars (e.g., Martínez-Vázquez et al. 2017; Hernitschek et al. 2019; Martínez-Vázquez et al. 2019; Muraveva et al. 2020; Nagarajan et al. 2022). Unfortunately, no RR Lyrae have been identified in Ret II (Vivas et al. 2020). The other features in the CMD for an old metal-poor stellar population that are good distance indicators are the MSTO and the horizontal branch. Following Brown et al. (2014) and Simon et al. (2021), we simultaneously fit the MS of Ret II with a Victoria–Regina isochrone (VandenBerg et al. 2014) and the two BHB stars with the horizontal branch of the old metal-poor globular cluster M92 (see Figure 1). We assumed a distance modulus of 14.62 mag (Del Principe et al. 2005; Sollima et al. 2006; Paust et al. 2007) and foreground reddening of $E(B-V)=0.023$ mag (Schlegel et al. 1998) for M92. For the theoretical isochrone, we assumed an age of 13 Gyr and the metallicity distribution described below, as well as a binary fraction of 0.48 (Geha et al. 2013). We found a distance modulus for Ret II of $m-M=17.50$ mag ($d=31.6$ kpc) and reddening of $E(B-V)=0.052$ mag.[61] As in our previous analyses, we assumed uncertainties of 0.07 mag in the distance modulus and 0.01 mag in $E(B-V)$. The distance of Ret II is in excellent agreement with the measurements of Mutlu-Pakdil et al. (2018) and Bechtol et al. (2015), although our reddening value is substantially larger.

For the metallicity distribution function (MDF) of Ret II, we relied on the spectroscopic sample of 16 stars with Ca triplet–based metallicities from Simon et al. (2015a). The other previously published studies of Ret II contain the same or smaller samples of member stars (Koposov et al. 2015; Ji et al. 2016a; Roederer et al. 2016). Under the assumption of a Gaussian MDF, Simon et al. (2015a) determined that the width of the distribution is $\sigma_{[Fe/H]}=0.28\pm0.09$ dex. The most recent spectroscopic analysis by Ji et al. (2022) included a larger set of Ret II members, but their Fe abundances are based on a single line, and many of the stars have only upper limits on [Fe/H]. Nevertheless, their Gaussian MDF agreed with that of Simon et al. (2015a), finding $\sigma_{/}=0.32^{+0.10}_{-0.07}$ dex.

[61] For comparison, the reddening at the center of Ret II, according to Schlafly & Finkbeiner (2011), is $E(B-V)=0.016$ mag. The reddening values determined for the other UFDs analyzed by Brown et al. (2014) and Simon et al. (2021), with the same methodology, were also larger than indicated by dust maps.

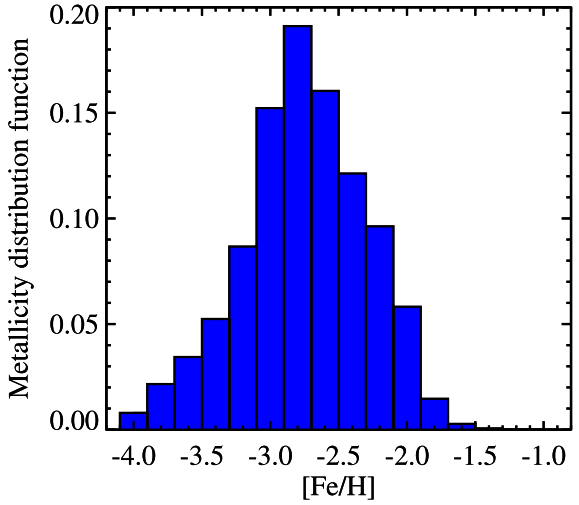

Figure 2. Metallicity distribution of Ret II, as determined from the spectroscopic metallicity measurements of Simon et al. (2015a). Each individual stellar metallicity is modeled as a Gaussian probability distribution, and samples are drawn from the combined probability distribution from all 16 stars.

To convert these metallicity measurements into an MDF without the assumption of an overall Gaussian shape, we modeled the metallicity of each star as a Gaussian probability distribution, constructed the cumulative distribution of the full set of metallicities, and then drew 16 samples from the cumulative distribution. Repeating this process 10^5 times, we built up a binned MDF for Ret II (see Figure 2). As described by Simon et al. (2021), this process produces an MDF that is somewhat broader than the true metallicity distribution, because it convolves the intrinsic MDF of the galaxy with the observational uncertainties. Given the observed width of the Ret II MDF (Simon et al. 2015a), though, we do not expect this broadening to have a significant effect. In addition, we note that although the MDF constrains the set of isochrones used to model the SFH, the position of old isochrones in the F606W–F814W CMD is a very weak function of the metallicity at [Fe/H]<-2.

3.2. SFH Modeling

As a starting point, we modeled the SFH of Ret II using the same techniques as Brown et al. (2014) and Simon et al. (2021), to which the reader should refer for more details. We created a Hess diagram from the ACS CMD, with bins of 0.02 mag in both color and magnitude. We used Besançon model simulations (Robin et al. 2003) to evaluate the contamination from foreground Milky Way stars in the ACS photometry. Given the large area covered by the HST mosaic, the estimated contamination in the region occupied by the Ret II stars was 3.5%. To determine the ages, we built model Hess diagrams based on linear combinations of Victoria–Regina isochrones, assuming the best-fit values of the initial mass function and binary fraction determined by Geha et al. (2013) for Hercules,[62] and applying the constraints that the combination must have a metallicity distribution matching the observed MDF and that the metallicity must increase with time. The isochrone grid used for the synthetic Hess diagrams

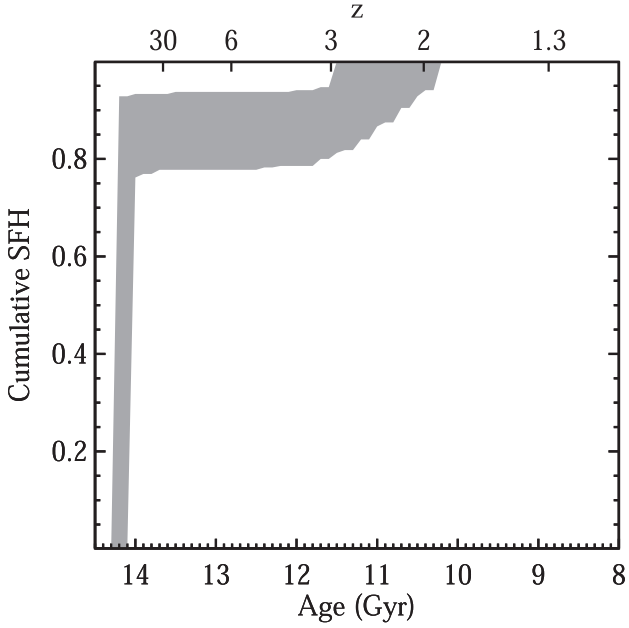

Figure 3. SFH of Ret II, with a model consisting of two instantaneous bursts. This figure can be directly compared to the SFHs of other UFDs as determined by Brown et al. (2014).

spanned from [Fe/H] $= -4$ to [Fe/H] $= -1$ in metallicity and 8–14.5 Gyr in age.[63] We then fit the observed Hess diagram with the set of models in a region around the MSTO, using the Poisson likelihood ratio from Dolphin (2002).

Based on our previous work, our initial model for the Ret II SFH consisted of two instantaneous bursts of star formation, with the timing of the bursts and the fraction of stars formed in each burst being free parameters. In this model, the best fit consisted of a burst that occurred 14.1 Gyr ago, containing 87.5% of the stars, and a second burst at 10.7 Gyr ago, with the remaining 12.5% of the stars. The range of SFHs for Ret II in this model is shown in Figure 3, where the shaded region is based on the set of parameters that produce fit results within 1σ of the single best fit. This SFH is similar to those determined for Canes Venatici II and Coma Berenices by Brown et al. (2014), with $\gtrsim$80% of the stars formed nearly immediately after the Big Bang and the possibility of a small fraction forming up to a few Gyr later. As described in footnote, [64] an age older than 14 Gyr for these UFDs should not be taken as an indication of an inconsistency with the age of the universe, according to current cosmological models, but simply as an indication that the star formation in these systems began $\sim$1 Gyr earlier than in M92. Our Ret II SFH also agrees within the uncertainties with the measurements from the independent HST photometry of Sacchi et al. (2021).

Because our goal in this study is to constrain the timing of the *r*-process enrichment of Ret II, which cannot be accomplished when >80% of the stars form instantaneously, we also

[62] The Safarzadeh et al. (2022) measurements of the initial mass function and binary fraction for Ret II are consistent with the Geha et al. (2013) results for Hercules.

[63] Although 14.5 Gyr is nominally older than the age of the universe in the standard cosmology, as discussed by Brown et al. (2014), the ages in this paper should be regarded as ages relative to a model in which the age of M92 is 13.2 Gyr.

[64] Although 14.5 Gyr is nominally older than the age of the universe in the standard cosmology, as discussed by Brown et al. (2014), the ages in this paper should be regarded as ages relative to a model in which the age of M92 is 13.2 Gyr.

considered models in which the two bursts[65] have nonzero durations. Brown et al. (2014) tried similar models for the six UFDs that they analyzed, finding that increasing the burst duration did not improve the fits, but in the case of Ret II we obtained a different result. To establish reasonable boundaries for the parameter space, motivated by the results of the instantaneous burst model fit above, we imposed these conditions: (1) the first burst began between 11.5 and 14.5 Gyr ago; (2) the duration of the first burst was 0–3 Gyr, if it started 11.5–13.5 Gyr ago, or 0–5 Gyr, if it started 13.5–14.5 Gyr ago; (3) the second burst began between the start of the first burst and 8 Gyr ago; and (4) the second burst could have a duration up to 3 Gyr, but it must have ended by 8 Gyr ago (e.g., a burst that started at 8.5 Gyr could only last for 0.5 Gyr). The limit of no star formation more recent than 8 Gyr ago was based on the results obtained with the instantaneous burst model. With this extended burst model, the best fit consisted of one burst beginning 14.3 Gyr ago and continuing for 2.6 Gyr, comprising 56% of the stars, and a second short burst beginning 14.2 Gyr ago, lasting 100 Myr, and containing 44% of the stars. We emphasize, though, that many other combinations of two bursts are also consistent with the data, including those with both burst durations significantly exceeding 100 Myr. Unlike the modeling of the other UFDs, for Ret II, the extended bursts produced an SFH with a maximum likelihood score that was 1.4σ better than that achieved by the instantaneous burst model. Because the extended burst model used five free parameters, whereas the instantaneous burst model had three free parameters, it is worth noting that the extended burst fit is superior even if one penalizes for the number of free parameters, using either the Bayesian Information Criterion or the Akaike Information Criterion.

Although we do find evidence for temporally extended star formation in Ret II, the available data do not enable us to select a single unique combination of burst timing and duration. To illustrate some of the degeneracies in the fit results, in Figure 4, we show the MSTO region of the Ret II CMD, accompanied by isochrones spanning a range of ages for the most metal-poor and most metal-rich stars in Ret II. The photometric uncertainties for the individual stars in this magnitude range correspond to age uncertainties (at constant metallicity) of $\gtrsim$500 Myr and metallicity uncertainties (at constant age) of $\gtrsim$0.2 dex. With spectroscopic metallicity measurements for individual MSTO stars (recall that the existing MDF is determined entirely from brighter red giants), it may be possible to derive improved constraints on the Ret II SFH.

The early SFH of Ret II in the extended burst model is illustrated in Figure 5. Here, we examine the durations of the star formation for all of the models with maximum likelihood scores within 1σ of the best-fit model. Note that in this comparison, since the oldest bursts of star formation do not start at the same times in all of the models, we rely explicitly on relative ages, normalized to the onset of the star formation in each model. These results show that 28% of the total stellar mass of Ret II, matching the fraction of non-*r*-process-enhanced stars in the galaxy, had formed by 500 ± 200 Myr after the system began to form stars.

[65] Although we continue to use the term "burst" in this context, simulations suggest that such an extended star formation episode likely consists of a number of discrete bursts interspersed with quiescent periods, as a result of stellar feedback (e.g., Jeon et al. 2017; Wheeler et al. 2019).

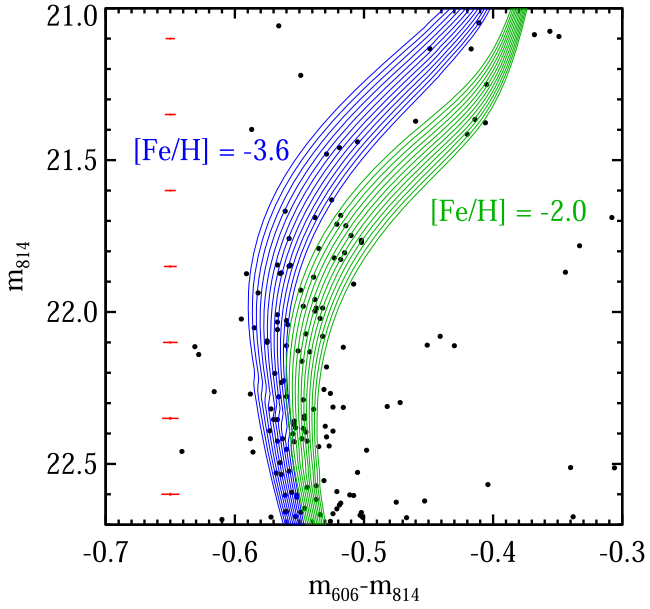

Figure 4. Turnoff region of the Ret II CMD in comparison to theoretical isochrones. The ranges in age and metallicity covered by the full grid of isochrones are much larger than can be straightforwardly displayed in a single figure, so here we have selected metallicities representing the extremes of the Ret II MDF. The blue curves are Victoria–Regina isochrones at [Fe/H] = −3.6 and the green curves are isochrones at [Fe/H] = −2.0. For each metallicity, 12 ages are shown in 200 Myr intervals, from 12.1 Gyr (the leftmost isochrone) to 14.3 Gyr (the rightmost isochrone). The typical photometric uncertainties are displayed in red along the left edge of the CMD.

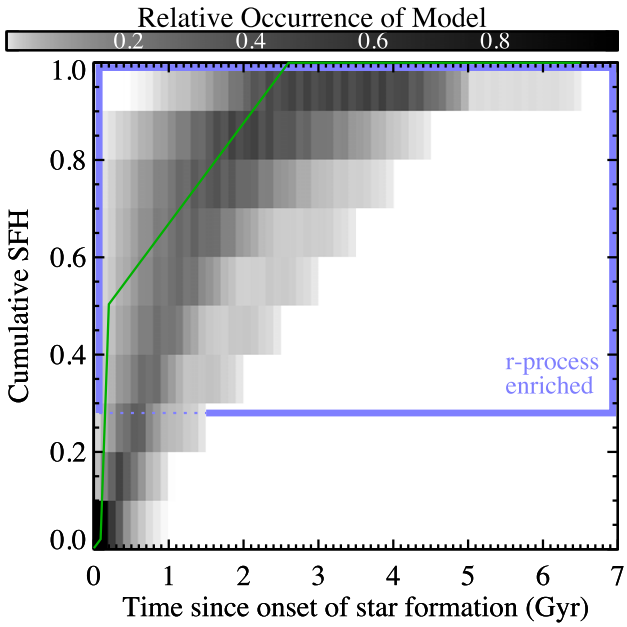

Figure 5. The buildup of stars early in the history of Ret II in the extended burst model. The grayscale represents the density of the models passing through a given point, with black indicating 100% of the models and white indicating 0% (i.e., points that are not consistent with any of the models). The models included in this figure are those with maximum likelihood scores within 1σ of the overall best fit. Unlike the quasi-absolute ages shown in Figure 3, in this plot, the *x*-axis uses relative ages, where the beginning of the star formation in each model is defined to occur at time = 0 Gyr. The green line displays the single best-fit model, which reaches 28% of the stellar mass more quickly than the median of the acceptable models. The blue outline indicates the portion of the parameter space that is observed to be enriched in *r*-process elements. The time at which a model crosses the boundary into the blue region therefore indicates the latest point at which the *r*-process nucleosynthesis could have occurred.

We offer the results above with the caveat that the sample of stars near the MSTO of Ret II that are sensitive to the age of the system is small. With $M_V = -3.1 \pm 0.1$ (Mutlu-Pakdil et al. 2018), Ret II is more than a factor of 2 less luminous than any of the UFDs that we have previously analyzed (Brown et al. 2012, 2014; Simon et al. 2021), with correspondingly fewer MSTO stars. The sparsest CMD in that set of galaxies belongs to Com ($M_V = -4.4$; Muñoz et al. 2018), which had 275 MSTO stars in the Brown et al. (2014) data set. The present Ret II observations include 176 stars along the MS and subgiant branch between $m_{814} = 21.0$ and $m_{814} = 22.7$. Although a larger sample would clearly be beneficial, our ACS coverage already includes essentially the entire area within the half-light radius of the galaxy, and extends to $\sim 1.4 r_{\rm half}$ along the major axis (Safarzadeh et al. 2022). Assuming an exponential radial profile (Mutlu-Pakdil et al. 2018), we estimate that the ACS mosaic includes 68% of the stars in Ret II, down to the magnitude limit of the data. Thus, even observing the entire area of Ret II out to $>3 r_{\rm half}$ (as would be straightforward with, e.g., the Roman Space Telescope; Wang et al. 2022) would increase the number of Ret II stars by no more than ∼50%, still resulting in a smaller sample of stars than was obtained for Com. Moreover, the number of foreground stars contaminating the CMD would increase linearly with the observed area, so the contamination of Ret II by Milky Way stars would worsen with wider coverage.

4. Analysis and Implications

4.1. Constraints on r-process Nucleosynthesis

In the largest spectroscopic study of Ret II, 72^{+10}_{-12}% of the stars in the galaxy were classified as *r*-process-rich (Ji et al. 2022). Because the ejecta from the event that produced the *r*-process elements in Ret II may have taken some time to uniformly enrich the entire interstellar medium of the galaxy, this measurement places an upper limit of 28^{+12}_{-10}% on the portion of Ret II stars that could have formed before the *r*-process event. In principle, if the enrichment was initially quite inhomogeneous and the mixing time was long, the fraction of stars forming before the event could have been considerably lower.

We therefore use the SFH of Ret II from Section 3.2 to place a limit on when the *r*-process enrichment must have occurred. As shown in Figure 5, 28% of the stars had formed within 500 ± 200 Myr of the onset of the star formation in Ret II. Thus, the *r*-process nucleosynthesis in Ret II must have occurred no more than 500 ± 200 Myr after its first stars formed. This result is consistent with the star formation and chemical enrichment timescales seen in hydrodynamic simulations of UFDs. Specifically, Tarumi et al. (2020) found that the complete mixing of *r*-process ejecta from a neutron star merger occurs within 250 Myr, and Jeon et al. (2021) showed that exclusively *r*-process-rich stars are formed less than 100 Myr after the merger event. Although the present observational limit is not strongly constraining in this context, it does demonstrate that long delay times of $\gtrsim$3 Gyr, such as those inferred for the only confirmed neutron star merger, GW170817 (e.g., Blanchard et al. 2017; Pan et al. 2017), are incompatible with the enrichment of Ret II.

The distribution of the delay times between the formation of a binary neutron star system and its eventual merger is currently poorly known (e.g., Mennekens & Vanbeveren 2016; Blanchard et al. 2017; Safarzadeh & Berger 2019; Skúladóttir & Salvadori 2020). However, chemical abundances in both the Milky Way and dwarf galaxies suggest that *r*-process nucleosynthesis (whether from merging neutron stars or not) must occur rapidly in some cases (e.g., Beniamini & Piran 2019; Simonetti et al. 2019; Skúladóttir & Salvadori 2020). Galaxy formation simulations also support rapid *r*-process enrichment (e.g., van de Voort et al. 2020; Jeon et al. 2021). Among the possible progenitor systems that could lead to *r*-process element production, rare core-collapse SNe, such as collapsars or magnetorotationally driven SNe, would create *r*-process material within ∼10 Myr, entirely consistent with the SFH limits for Ret II. Assuming a Salpeter (1955) initial mass function for stars above 1 $M_\odot$, the total number of core-collapse SNe between 8 and 50 $M_\odot$ in Ret II would be ∼180, with ∼20 of these at masses above the 28 $M_\odot$ threshold suggested by Taddia et al. (2019) and Barnes & Metzger (2022) for some collapsars. Rare core-collapse SNe are therefore plausible in Ret II from the perspective of stellar populations as well. Neutron star mergers are also very likely to be compatible with Ret II, so long as the initial conditions of the binary neutron stars allow them to merge within ∼500 Myr (Beniamini & Piran 2019; Safarzadeh et al. 2019; Andrews et al. 2020). Despite this presumed consistency with neutron star merger timescales, it is worth noting that the observed lanthanide fraction for Ret II stars is much higher than that inferred for GW170817, so if Ret II was enriched by a neutron star merger, then there must be a large range in lanthanide fractions for different merger events (Ji et al. 2019).

One additional scenario for the *r*-process nucleosynthesis in Ret II that could be considered is that the *r*-process elements were produced directly by Population III (Pop III) stars (e.g., Roederer et al. 2014; Mardini et al. 2020). This connection between early *r*-process enrichment and the first stars might be expected if, for example, collapsars are a major *r*-process site and the Pop III initial mass function was top-heavy (e.g., Bromm et al. 1999; Nakamura & Umemura 2001; Stacy et al. 2016, 2022). In that case, the occurrence of a collapsar would be more likely, both because of the increased number of massive stars per stellar mass formed and because Pop III stars likely have lower mass-loss rates, so they can retain the high masses and high angular momentum needed for collapsars (as well as jet-driven SNe). If no low-mass ($\lesssim$0.8 $M_\odot$) Pop III stars were formed in Ret II, then the first generation of stars would have left behind only chemical signatures, without contributing to the present-day stellar population of the galaxy. In this case, simulations suggest a delay of up to ∼100 Myr before the formation of the first metal-enriched stars (Magg et al. 2022), which would not be detectable as part of the overall delay time between the production of *r*-process material and the formation of the *r*-process-enhanced stars, given the methodology we used in Section 3.2. However, this course of events would make it difficult to explain the uniformity of the *r*-process enrichment among the bulk of the Ret II stars (Ji et al. 2022), which requires the complete mixing of the earlier nucleosynthetic products, as well as the 28% of the stars where neutron-capture species have not been detected. The very low *r*-process abundances in the latter set of stars require substantial inhomogeneities in the star-forming gas within Ret II, or perhaps these stars were originally formed in a different dwarf galaxy that did not feature a prolific *r*-process event, and were later accreted by Ret II.

4.2. The Quenching of Ret II

As mentioned in Section 3.2, the SFH of Ret II, when fit with the instantaneous burst model, closely resembles those of the lowest-luminosity members of the Brown et al. (2014) sample, Com ($M_V = -4.4$), Leo IV ($M_V = -5.0$), and CVn II ($M_V = -5.2$). These galaxies each formed $\gtrsim$80% of their stars in an initial burst before reionization and have mean ages of >13 Gyr. A small amount of star formation as late as $z = 2$ ($\sim$10.5 Gyr ago) cannot be ruled out in any of these systems. The Ret II SFH shown in Figure 3 is similar both qualitatively and quantitatively, with a mean age of 13.7 ± 0.2 Gyr and more than 80% of its stellar mass in place at the earliest ages (>12 Gyr ago). On the other hand, our Ret II models prefer not to have 100% of the stars forming by $z = 6$, whereas that SFH is allowed for each of the other UFDs listed above.

The Ret II SFH is consistent with the general paradigm for quenching in UFDs, as discussed in previous papers, where the large majority of the star formation is complete before the end of reionization (e.g., Brown et al. 2014; Wheeler 2015; Rodriguez Wimberly et al. 2019; Applebaum et al. 2021; Sacchi et al. 2021; Simon et al. 2021). Based on its Gaia data release 2 proper motion, Fillingham et al. (2019) derived an infall time for Ret II of $10.2^{+1.1}_{-2.4}$ Gyr, which could be consistent with the final cessation of the star formation in Ret II, but occurred well after the star formation rate dropped to a small fraction of its peak value. We note that simulations show that the star formation in dwarf galaxies can continue at a low level for $\sim$1 Gyr after reionization, before the combination of heating and the lack of further accretion causes permanent quenching (e.g., Oñorbe 2015; Rey et al. 2019; Wheeler et al. 2019).

A trickle of late-time star formation is also consistent with the observed chemical evolution in Ret II. Ji et al. (2022) found that the most metal-rich star in Ret II has a very low [Mg/Ca] ratio, of the 10 stars with Mg and Ca constraints. A low [Mg/Ca] ratio in dwarf galaxies is often attributed to the integrated galactic initial mass function (McWilliam et al. 2013; Weidner et al. 2013), where the low total gas mass in a galaxy restricts the maximum mass of core-collapse SN progenitors and thus the amount of Mg produced. In this case, the fraction of low-[Mg/Ca] stars would be expected to match the fraction of post-reionization star formation in Ret II, consistent with our results.

Orbital studies including the gravitational potential of the LMC have suggested that it has a significant gravitational influence on Ret II, with Ret II being classified as a recently captured LMC satellite (Patel et al. 2020) or a long-standing member of the Magellanic group (Battaglia et al. 2022). In either case, the early environmental history of Ret II may be more difficult to untangle than previously assumed. Nevertheless, the conclusion of Rodriguez Wimberly et al. (2019) that UFDs as a group cannot be primarily quenched by environmental processes still holds, and is perhaps strengthened by the addition of Ret II to the set of galaxies with well-determined SFHs.

5. Conclusions

We have derived the SFH of the UFD Ret II, using deep HST imaging covering most of the galaxy. Similar to previously studied UFDs, we find that the galaxy is old, with most of its stars forming shortly after the Big Bang. A small minority of the stars (<15%) may have formed up to several Gyr later, at z $\sim$2.

Although the SFH can be described by a model consisting of two instantaneous bursts of star formation, we obtain slightly better fits by allowing each burst to be extended in time. With these extended bursts, the best fit consists of approximately half of the stars forming in a short (100 Myr) burst and the other half forming over a longer episode spanning 2.6 Gyr, both beginning at very early times. In this scenario, a broad range of model parameters produce fits of similar quality. Recalling that 28% of the stars in Ret II are lacking *r*-process elements, we find that across the full set of models consistent with the data, 28% of the stars had been formed at $t = 500 \pm 200$ Myr after the beginning of star formation. We therefore conclude that the *r*-process nucleosynthesis in the galaxy occurred no later than 500 ± 200 Myr after the first Ret II stars had been formed. This upper limit on the time delay between the initial star formation and the production of *r*-process material is consistent with either rare core-collapse SNe or a neutron star merger site for the *r*-process, with the constraint that the merger would need to occur relatively quickly in the latter case. *r*-process sources with long delay times ($\gtrsim$1 Gyr) are ruled out in Ret II.

The SFH of Ret II shows a sharp decline around or before the time of reionization, consistent with the possibility that photoheating from the increased UV radiation at that time was largely responsible for quenching the galaxy.

Despite the increase in the number of UFDs with detailed chemical abundance measurements over the last few years, the extreme *r*-process enrichment of Ret II has remained unique. The closest analog is Tucana III (Hansen et al. 2017; Marshall et al. 2019), but its *r*-process abundances are an order of magnitude lower and the classification of Tuc III as a dwarf galaxy has still not been confirmed (Simon et al. 2017; Baumgardt et al. 2022). Identifying additional examples of this phenomenon, especially among more luminous UFDs where the SFH can be determined more accurately, would be helpful for improving the constraint on the source of the *r*-process elements. In addition, it would be interesting to study the *r*-process abundances in more detail in UFDs that contain very little *r*-process material. If the fraction of stars containing any *r*-process elements in those galaxies can be measured as it has been for Ret II, new constraints on the low-yield *r*-process source could be obtained as well.

We thank the referee for suggestions that improved the presentation of our results. This publication is based upon work supported by Program No. HST-GO-14766, provided by NASA through a grant from the Space Telescope Science Institute, which is operated by the Association of Universities for Research in Astronomy, Incorporated, under NASA contract NAS5-26555. J.D.S. was also partially supported by the National Science Foundation, under grant AST-1714873. B.M.P. was supported by an NSF Astronomy and Astrophysics Postdoctoral Fellowship, under award AST-2001663. A.F. acknowledges support from NSF grant AST-1716251.

Funding for the DES Projects has been provided by the U.S. Department of Energy, the U.S. National Science Foundation, the Ministry of Science and Education of Spain, the Science and Technology Facilities Council of the United Kingdom, the Higher Education Funding Council for England, the National Center for Supercomputing Applications at the University of Illinois at Urbana-Champaign, the Kavli Institute of

Cosmological Physics at the University of Chicago, the Center for Cosmology and Astro-Particle Physics at the Ohio State University, the Mitchell Institute for Fundamental Physics and Astronomy at Texas A&M University, Financiadora de Estudos e Projetos, Fundação Carlos Chagas Filho de Amparo à Pesquisa do Estado do Rio de Janeiro, Conselho Nacional de Desenvolvimento Científico e Tecnológico and the Ministério da Ciência, Tecnologia e Inovação, the Deutsche Forschungsgemeinschaft, and the Collaborating Institutions in the Dark Energy Survey.

The Collaborating Institutions are Argonne National Laboratory, the University of California at Santa Cruz, the University of Cambridge, Centro de Investigaciones Energéticas, Medioambientales y Tecnológicas-Madrid, the University of Chicago, University College London, the DES-Brazil Consortium, the University of Edinburgh, the Eidgenössische Technische Hochschule (ETH) Zürich, Fermi National Accelerator Laboratory, the University of Illinois at Urbana-Champaign, the Institut de Ciències de l'Espai (IEEC/CSIC), the Institut de Física d'Altes Energies, Lawrence Berkeley National Laboratory, the Ludwig-Maximilians Universität München and the associated Excellence Cluster Universe, the University of Michigan, NSF's NOIRLab, the University of Nottingham, the Ohio State University, the University of Pennsylvania, the University of Portsmouth, SLAC National Accelerator Laboratory, Stanford University, the University of Sussex, Texas A&M University, and the OzDES Membership Consortium.

Based in part on observations at Cerro Tololo Inter-American Observatory at NSF's NOIRLab (NOIRLab Prop. ID 2012B-0001; PI: J. Frieman), which is managed by the Association of Universities for Research in Astronomy (AURA), under a cooperative agreement with the National Science Foundation.

The DES data management system is supported by the National Science Foundation under grant Nos. AST-1138766 and AST-1536171. The DES participants from Spanish institutions are partially supported by MICINN under grants ESP2017-89838, PGC2018-094773, PGC2018-102021, SEV-2016-0588, SEV-2016-0597, and MDM-2015-0509, some of which include ERDF funds from the European Union. IFAE is partially funded by the CERCA program of the Generalitat de Catalunya. Research leading to these results has received funding from the European Research Council, under the European Union's Seventh Framework Program (FP7/2007-2013), including ERC grant agreements 240672, 291329, and 306478. We acknowledge support from the Brazilian Instituto Nacional de Ciência e Tecnologia (INCT) do e-Universo (CNPq grant 465376/2014-2).

This manuscript has been authored by Fermi Research Alliance, LLC, under Contract No. DE-AC02-07CH11359 with the U.S. Department of Energy, Office of Science, Office of High Energy Physics.

This research has made use of NASA's Astrophysics Data System Bibliographic Services.

The HST data presented in this paper were obtained from the Mikulski Archive for Space Telescopes (MAST) at the Space Telescope Science Institute. The specific observations analyzed can be accessed via doi:10.17909/y62d-3794.

Facility: HST (ACS).

Software: DAOPHOT-II (Stetson 1987), DOLPHOT (Dolphin 2000).

ORCID iDs

Joshua D. Simon https://orcid.org/0000-0002-4733-4994
Thomas M. Brown https://orcid.org/0000-0002-1793-9968
Burçin Mutlu-Pakdil https://orcid.org/0000-0001-9649-4815
Alexander P. Ji https://orcid.org/0000-0002-4863-8842
Alex Drlica-Wagner https://orcid.org/0000-0001-8251-933X
Clara E. Martínez-Vázquez https://orcid.org/0000-0002-9144-7726
Ting S. Li https://orcid.org/0000-0002-9110-6163
Keith Bechtol https://orcid.org/0000-0001-8156-0429
Anna Frebel https://orcid.org/0000-0002-2139-7145
Marla Geha https://orcid.org/0000-0002-7007-9725
Terese T. Hansen https://orcid.org/0000-0001-6154-8983
Andrew B. Pace https://orcid.org/0000-0002-6021-8760
M. Aguena https://orcid.org/0000-0001-5679-6747
O. Alves https://orcid.org/0000-0002-7394-9466
J. Annis https://orcid.org/0000-0002-0609-3987
D. Bacon https://orcid.org/0000-0002-2562-8537
E. Bertin https://orcid.org/0000-0002-3602-3664
D. Brooks https://orcid.org/0000-0002-8458-5047
D. L. Burke https://orcid.org/0000-0003-1866-1950
A. Carnero Rosell https://orcid.org/0000-0003-3044-5150
M. Carrasco Kind https://orcid.org/0000-0002-4802-3194
J. Carretero https://orcid.org/0000-0002-3130-0204
M. Costanzi https://orcid.org/0000-0001-8158-1449
L. N. da Costa https://orcid.org/0000-0002-7731-277X
J. De Vicente https://orcid.org/0000-0001-8318-6813
S. Desai https://orcid.org/0000-0002-0466-3288
I. Ferrero https://orcid.org/0000-0002-1295-1132
J. García-Bellido https://orcid.org/0000-0002-9370-8360
D. W. Gerdes https://orcid.org/0000-0001-6942-2736
D. Gruen https://orcid.org/0000-0003-3270-7644
R. A. Gruendl https://orcid.org/0000-0002-4588-6517
J. Gschwend https://orcid.org/0000-0003-3023-8362
S. R. Hinton https://orcid.org/0000-0003-2071-9349
D. L. Hollowood https://orcid.org/0000-0002-9369-4157
K. Kuehn https://orcid.org/0000-0003-0120-0808
N. Kuropatkin https://orcid.org/0000-0003-2511-0946
J. L. Marshall https://orcid.org/0000-0003-0710-9474
J. Mena-Fernández https://orcid.org/0000-0001-9497-7266
R. Miquel https://orcid.org/0000-0002-6610-4836
F. Paz-Chinchón https://orcid.org/0000-0003-1339-2683
M. E. S. Pereira https://orcid.org/0000-0002-7131-7684
A. Pieres https://orcid.org/0000-0001-9186-6042
A. A. Plazas Malagón https://orcid.org/0000-0002-2598-0514
E. Sanchez https://orcid.org/0000-0002-9646-8198
I. Sevilla-Noarbe https://orcid.org/0000-0002-1831-1953
M. Smith https://orcid.org/0000-0002-3321-1432
M. E. C. Swanson https://orcid.org/0000-0002-1488-8552
G. Tarle https://orcid.org/0000-0003-1704-0781
C. To https://orcid.org/0000-0001-7836-2261
N. Weaverdyck https://orcid.org/0000-0001-9382-5199

References

Andrews, J. J., Breivik, K., Pankow, C., D'Orazio, D. J., & Safarzadeh, M. 2020, ApJL, 892, L9
Applebaum, E., Brooks, A. M., Christensen, C. R., et al. 2021, ApJ, 906, 96
Arcones, A., & Thielemann, F.-K. 2013, JPhG, 40, 013201
Barnes, J., & Metzger, B. D. 2022, ApJL, 939, L29

Bartos, I., & Márka, S. 2019, ApJL, 881, L4
Battaglia, G., Taibi, S., Thomas, G. F., & Fritz, T. K. 2022, A&A, 657, A54
Baumgardt, H., Faller, J., Meinhold, N., McGovern-Greco, C., & Hilker, M. 2022, MNRAS, 510, 3531
Bechtol, K., Drlica-Wagner, A., Balbinot, E., et al. 2015, ApJ, 807, 50
Beniamini, P., & Piran, T. 2019, MNRAS, 487, 4847
Blanchard, P. K., Berger, E., Fong, W., et al. 2017, ApJL, 848, L22
Brauer, K., Ji, A. P., Drout, M. R., & Frebel, A. 2021, ApJ, 915, 81
Bromm, V., Coppi, P. S., & Larson, R. B. 1999, ApJL, 527, L5
Brown, T. M., Tumlinson, J., Geha, M., et al. 2012, ApJL, 753, L21
Brown, T. M., Tumlinson, J., Geha, M., et al. 2014, ApJ, 796, 91
Burbidge, E. M., Burbidge, G. R., Fowler, W. A., & Hoyle, F. 1957, RvMP, 29, 547
Cameron, A. G. W. 2003, ApJ, 587, 327
Chiaki, G., & Wise, J. H. 2019, MNRAS, 482, 3933
Chornock, R., Berger, E., Kasen, D., et al. 2017, ApJL, 848, L19
Del Principe, M., Piersimoni, A. M., Bono, G., et al. 2005, AJ, 129, 2714
Dolphin, A. E. 2000, PASP, 112, 1383
Dolphin, A. E. 2002, MNRAS, 332, 91
Dominik, M., Belczynski, K., Fryer, C., et al. 2012, ApJ, 759, 52
Drlica-Wagner, A., Sevilla-Noarbe, I., Rykoff, E. S., et al. 2018, ApJS, 235, 33
Drout, M. R., Piro, A. L., Shappee, B. J., et al. 2017, Sci, 358, 1570
Fillingham, S. P., Cooper, M. C., Kelley, T., et al. 2019, MNRAS, submitted (arXiv:1906.04180)
Fitts, A., Boylan-Kolchin, M., Bullock, J. S., et al. 2018, MNRAS, 479, 319
Ford, H. C., Clampin, M., Hartig, G. F., et al. 2003, Proc. SPIE, 4854, 81
Fraser, J., & Schonrich, R. 2022, MNRAS, 509, 6008
Frebel, A. 2018, ARNPS, 68, 237
Frebel, A., Simon, J. D., Geha, M., & Willman, B. 2010, ApJ, 708, 560
Frebel, A., Simon, J. D., & Kirby, E. N. 2014, ApJ, 786, 74
Fujimoto, S.-i., Nishimura, N., & Hashimoto, M.-a. 2008, ApJ, 680, 1350
Gaia Collaboration, Vallenari, A., Brown, A. G. A., et al. 2022, arXiv:2208.00211
Geha, M., Brown, T. M., Tumlinson, J., et al. 2013, ApJ, 771, 29
Griffen, B. F., Dooley, G. A., Ji, A. P., et al. 2018, MNRAS, 474, 443
Halevi, G., & Mösta, P. 2018, MNRAS, 477, 2366
Hansen, T. T., Simon, J. D., Marshall, J. L., et al. 2017, ApJ, 838, 44
Hartwig, T., Ishigaki, M. N., Klessen, R. S., & Yoshida, N. 2019, MNRAS, 482, 1204
Hernitschek, N., Cohen, J. G., Rix, H.-W., et al. 2019, ApJ, 871, 49
Ishigaki, M. N., Aoki, W., Arimoto, N., & Okamoto, S. 2014, A&A, 562, A146
Jeon, M., Besla, G., & Bromm, V. 2017, ApJ, 848, 85
Jeon, M., Besla, G., & Bromm, V. 2021, MNRAS, 506, 1850
Ji, A. P., Drout, M. R., & Hansen, T. T. 2019, ApJ, 882, 40
Ji, A. P., Frebel, A., Chiti, A., & Simon, J. D. 2016a, Natur, 531, 610
Ji, A. P., Frebel, A., Simon, J. D., & Chiti, A. 2016b, ApJ, 830, 93
Ji, A. P., Frebel, A., Simon, J. D., & Geha, M. 2016c, ApJ, 817, 41
Ji, A. P., Simon, J. D., Roederer, I. U., et al. 2022, AJ, in press (arXiv:2207.03499)
Kasliwal, M. M., Nakar, E., Singer, L. P., et al. 2017, Sci, 358, 1559
Koposov, S. E., Belokurov, V., Torrealba, G., & Evans, N. W. 2015, ApJ, 805, 130
Lattimer, J. M., & Schramm, D. N. 1974, ApJL, 192, L145
MacFadyen, A. I., & Woosley, S. E. 1999, ApJ, 524, 262
Magg, M., Reis, I., Fialkov, A., et al. 2022, MNRAS, 514, 4433
Mardini, M. K., Placco, V. M., Meiron, Y., et al. 2020, ApJ, 903, 88
Marshall, J. L., Hansen, T., Simon, J. D., et al. 2019, ApJ, 882, 177
Martínez-Vázquez, C. E., Monelli, M., Bernard, E. J., et al. 2017, ApJ, 850, 137
Martínez-Vázquez, C. E., Vivas, A. K., Gurevich, M., et al. 2019, MNRAS, 490, 2183
McWilliam, A., Wallerstein, G., & Mottini, M. 2013, ApJ, 778, 149
Mennekens, N., & Vanbeveren, D. 2016, A&A, 589, A64
Meyer, B. S. 1989, ApJ, 343, 254
Muñoz, R. R., Côté, P., Santana, F. A., et al. 2018, ApJ, 860, 66
Muraveva, T., Clementini, G., Garofalo, A., & Cusano, F. 2020, MNRAS, 499, 4040
Mutlu-Pakdil, B., Sand, D. J., Carlin, J. L., et al. 2018, ApJ, 863, 25
Mutlu-Pakdil, B., Sand, D. J., Crnojević, D., et al. 2020, ApJ, 902, 106
Mutlu-Pakdil, B., Sand, D. J., Walker, M. G., et al. 2019, ApJ, 885, 53
Nagarajan, P., Weisz, D. R., & El-Badry, K. 2022, ApJ, 932, 19
Nakamura, F., & Umemura, M. 2001, ApJ, 548, 19
Oñorbe, J., Boylan-Kolchin, M., Bullock, J. S., et al. 2015, MNRAS, 454, 2092
Pan, Y. C., Kilpatrick, C. D., Simon, J. D., et al. 2017, ApJL, 848, L30
Patel, E., Kallivayalil, N., Garavito-Camargo, N., et al. 2020, ApJ, 893, 121
Paust, N. E. Q., Chaboyer, B., & Sarajedini, A. 2007, AJ, 133, 2787
Pian, E., D'Avanzo, P., Benetti, S., et al. 2017, Natur, 551, 67
Reggiani, H., Schlaufman, K. C., Casey, A. R., Simon, J. D., & Ji, A. P. 2021, AJ, 162, 229
Rey, M. P., Pontzen, A., Agertz, O., et al. 2019, ApJL, 886, L3
Robin, A. C., Reylé, C., Derrière, S., & Picaud, S. 2003, A&A, 409, 523
Rodriguez Wimberly, M. K., Cooper, M. C., Fillingham, S. P., et al. 2019, MNRAS, 483, 4031
Roederer, I. U., Mateo, M., Bailey, J. I., III, et al. 2016, AJ, 151, 82
Roederer, I. U., Preston, G. W., Thompson, I. B., Shectman, S. A., & Sneden, C. 2014, ApJ, 784, 158
Sacchi, E., Richstein, H., Kallivayalil, N., et al. 2021, ApJL, 920, L19
Safarzadeh, M., & Berger, E. 2019, ApJL, 878, L12
Safarzadeh, M., Ramirez-Ruiz, E., Andrews, J. J., et al. 2019, ApJ, 872, 105
Safarzadeh, M., Simon, J. D., & Loeb, A. 2022, ApJ, 930, 54
Salpeter, E. E. 1955, ApJ, 121, 161
Schlafly, E. F., & Finkbeiner, D. P. 2011, ApJ, 737, 103
Schlegel, D. J., Finkbeiner, D. P., & Davis, M. 1998, ApJ, 500, 525
Siegel, D. M., Barnes, J., & Metzger, B. D. 2019, Natur, 569, 241
Simon, J. D., Brown, T. M., Drlica-Wagner, A., et al. 2021, ApJ, 908, 18
Simon, J. D., Drlica-Wagner, A., Li, T. S., et al. 2015a, ApJ, 808, 95
Simon, J. D., Jacobson, H. R., Frebel, A., et al. 2015b, ApJ, 802, 93
Simon, J. D., Li, T. S., Drlica-Wagner, A., et al. 2017, ApJ, 838, 11
Simonetti, P., Matteucci, F., Greggio, L., & Cescutti, G. 2019, MNRAS, 486, 2896
Skúladóttir, Á, & Salvadori, S. 2020, A&A, 634, L2
Sollima, A., Cacciari, C., & Valenti, E. 2006, MNRAS, 372, 1675
Stacy, A., Bromm, V., & Lee, A. T. 2016, MNRAS, 462, 1307
Stacy, A., McKee, C. F., Lee, A. T., Klein, R. I., & Li, P. S. 2022, MNRAS, 511, 5042
Stetson, P. B. 1987, PASP, 99, 191
Surman, R., McLaughlin, G. C., & Hix, W. R. 2006, ApJ, 643, 1057
Taddia, F., Sollerman, J., Fremling, C., et al. 2019, A&A, 621, A71
Tanvir, N. R., Levan, A. J., González-Fernández, C., et al. 2017, ApJL, 848, L27
Tarumi, Y., Yoshida, N., & Inoue, S. 2020, MNRAS, 494, 120
VandenBerg, D. A., Bergbusch, P. A., Ferguson, J. W., & Edvardsson, B. 2014, ApJ, 794, 72
van de Voort, F., Pakmor, R., Grand, R. J. J., et al. 2020, MNRAS, 494, 4867
Vivas, A. K., Martínez-Vázquez, C., & Walker, A. R. 2020, ApJS, 247, 35
Wang, Y., Zhai, Z., Alavi, A., et al. 2022, ApJ, 928, 1
Weidner, C., Kroupa, P., Pflamm-Altenburg, J., & Vazdekis, A. 2013, MNRAS, 436, 3309
Wheeler, C., Hopkins, P. F., Pace, A. B., et al. 2019, MNRAS, 490, 4447
Wheeler, C., Oñorbe, J., Bullock, J. S., et al. 2015, MNRAS, 453, 1305